Appl. Phys. B (2016) 122:292
DOI 10.1007/s00340-016-6569-7

Applied Physics B
Lasers and Optics

Sensitivity and resolution in frequency comb spectroscopy of buffer gas cooled polyatomic molecules

P. Bryan Changala[1] · Ben Spaun[1] · David Patterson[2] · John M. Doyle[2] · Jun Ye[1]

Received: 8 August 2016 / Accepted: 4 November 2016 / Published online: 26 November 2016

Abstract We discuss the use of cavity-enhanced direct frequency comb spectroscopy in the mid-infrared region with buffer gas cooling of polyatomic molecules for high-precision rovibrational absorption spectroscopy. A frequency comb coupled to an optical enhancement cavity allows us to collect high-resolution, broad-bandwidth infrared spectra of translationally and rotationally cold (10–20 K) gas-phase molecules with high absorption sensitivity and fast acquisition times. The design and performance of the combined apparatus are discussed in detail. Recorded rovibrational spectra in the CH stretching region of several organic molecules, including vinyl bromide (CH_2CHBr), adamantane ($C_{10}H_{16}$), and diamantane ($C_{14}H_{20}$) demonstrate the resolution and sensitivity of this technique, as well as the intrinsic challenges faced in extending the frontier of high-resolution spectroscopy to large complex molecules.

1 Introduction

The development of the optical frequency comb has dramatically changed the field of precision metrology and spectroscopy [1, 2]. While the use of combs as frequency references is now ubiquitous, they can also be directly employed for optical spectroscopy using techniques known as direct frequency comb spectroscopy [3]. By coupling frequency combs to high-finesse optical cavities, cavity-enhanced direct frequency comb spectroscopy (CE-DFCS) combines broad spectral bandwidth, high spectral resolution, and high detection sensitivity [4, 5].

The extension of CE-DFCS to the mid-infrared spectral region has provided a powerful new tool for rovibrational molecular spectroscopy, with recent demonstrations of trace gas detection [6] and time-resolved spectroscopy of transient radicals [7]. However, up to now mid-infrared CE-DFCS studies have been limited to small, simple molecules in order to avoid spectral congestion. Consequently, such studies have not taken full advantage of the high spectral resolution afforded by the narrow linewidth of individual comb modes. One primary challenge to studying more complex molecules is that those with more than ~ten atoms have intractably congested absorption spectra at room temperature, precluding high-resolution studies. We have recently addressed this issue by combining mid-infrared CE-DFCS with buffer gas cooling of complex polyatomic molecules [8]. By cooling molecules' translational and rotational temperatures to 10−20 K, rovibrational spectra are drastically simplified, exhibiting narrow Doppler linewidths, reduced spectral congestion, and enhanced absorption cross sections. In contrast to supersonic expansion jets [9, 10], buffer gas cooling [11–14] provides a continuous source of cold molecules with slow laboratory frame velocities and long interaction times. The modest gas throughput obviates the need for significant pumping infrastructure. This method has permitted the measurement of the first rotationally resolved absorption spectra in the CH stretching region (~3 μm) of several large organic

This article is part of the topical collection "Enlightening the World with the Laser" - Honoring T. W. Hänsch guest edited by Tilman Esslinger, Nathalie Picqué, and Thomas Udem.

✉ P. Bryan Changala
bryan.changala@colorado.edu

[1] JILA, National Institute of Standards and Technology and University of Colorado, Department of Physics, University of Colorado, Boulder, CO 80309, USA

[2] Department of Physics, Harvard University, Cambridge, MA 02138, USA

molecules, with all the benefits of sensitivity and fast acquisition times provided by CE-DFCS.

In this article, we provide a detailed description of the design and performance of our buffer gas cooling frequency comb spectrometer. Selected spectroscopic studies are discussed that illustrate both the capabilities of this technique, as well as more general prospects for high-resolution rovibrational spectroscopy of complex polyatomic molecules. We report spectra in the CH stretching region of vinyl bromide, CH_2CHBr, where we readily resolve small isotope splittings and nuclear hyperfine structure. Accurate relative transition intensities are shown to be measured over broad spectral bandwidths. We also discuss the spectra of two large molecules: adamantane, $C_{10}H_{16}$, and diamantane, $C_{14}H_{20}$, the simplest two diamonoid molecules, as an example of the onset of intramolecular vibrational redistribution (IVR) [15]. While the spectrum of adamantane displays well-resolved rotational structure at internal energies of $\sim 3000\ cm^{-1}$, intrinsic spectral congestion caused by IVR renders that of diamantane essentially continuous. This observation has important implications for high-resolution spectroscopy of molecules of this size or larger at the internal energies probed here.

2 Apparatus and methods

2.1 Frequency comb light source

The mid-infrared frequency comb is generated in a tunable optical parametric oscillator (OPO) synchronously pumped by a 1 μm ytterbium (Yb) fiber comb [16]. The 1 μm pump comb has a repetition rate $f_{rep} \approx 136.6$ MHz and a maximum output power of 10 W. The OPO is based on a fan-out MgO-doped periodically poled lithium niobate (PPLN) crystal within a cavity that is singly resonant at the signal wavelength. By tuning the quasi-phase-matching period of the fan-out PPLN crystal, idler output is generated with a center wavelength from 2.8 to 4.8 μm, a maximum average power of 1.5 W, and a simultaneous bandwidth up to 0.3 μm. The experiments reported here use idler light from 3.0 to 3.3 μm with an average power ranging from 100 to 300 mW.

The optical frequency of each comb mode is determined by $\nu_n = f_{ceo} + nf_{rep}$, where n is the integer comb mode number of order 10^5–10^6. Stabilization of the optical frequency requires locking both the carrier-envelope offset frequency f_{ceo} and the repetition rate f_{rep} of the idler comb. We lock f_{rep} by picking off a small portion of the 1 μm ytterbium fiber comb and measuring its repetition rate directly on a fast photodiode. The seventh harmonic of the repetition rate $7f_{rep} \approx 956$ MHz is mixed with a stable 1 GHz Wenzel quartz oscillator, slowly slaved to a 10 MHz cesium (Cs) clock. The resulting beat note is used to generate a phase error signal with respect to the RF output of a direct digital synthesizer (DDS), which is phase locked to the same RF oscillator. This error signal is then used to feed back simultaneously on a fast piezo (PZT)-actuated cavity mirror and a slower PZT fiber stretcher in the fiber laser oscillator.

The f_{ceo} frequency of the mid-IR idler comb is measured by performing an optical beat note between the 1 μm pump light (p) and the parasitic sum frequency of the pump and idler ($p + i$) generated by the OPO crystal. A 150- to 200-mW portion of the pump light is picked off and coupled into a 15-cm-long piece of highly nonlinear supercontinuum fiber to broaden it to ~780 nm in order to be spectrally overlapped with the $p + i$ light. The output of the supercontinuum fiber and the $p + i$ light are then spatially and temporally overlapped onto a single photodiode to measure the $p - (p + i)$ optical beat note, which is equal to f_{ceo} of the idler comb. This RF is used to generate a phase error signal with another DDS set to the desired f_{ceo} value. The error signal is fed back onto PZT-actuated mirrors in the OPO cavity.

2.2 Buffer gas cooled molecule source and enhancement cavity

Cryogenic cooling is achieved with a liquid-helium cryostat refrigerator placed within a vacuum dewar chamber. Figure 1a shows a schematic of the apparatus. A $(6\ cm)^3$ aluminum cell is anchored to the 4 K stage of the refrigerator and reaches wall temperatures of 5−10 K, depending on residual blackbody and molecule flow heat loads. The cold cell is surrounded by a 35 K copper shield to reduce radiative blackbody heating. A small continuous flow (~10 sccm) of helium buffer gas is pre-cooled to 4 K before entering the cold cell, where it builds up a steady-state density of $\sim 10^{14}\ cm^{-3}$. Helium that escapes the cell is cryopumped by charcoal sorbs attached to the 4 K stage. The sorbs have sufficient capacity to pump helium for several hours before requiring a warm-up to allow for helium desorption.

Warm gas-phase molecules enter the cold cell through a ~1-cm aperture in the cell wall. After many helium-molecule and helium-cell collisions, the molecular translational and rotational degrees of freedom are brought into quasi-thermal equilibrium with the cold cell wall. Measured rotational and translational temperatures are typically 10−20 K. For volatile molecules with sufficient vapor pressure at room temperature, a flow of 1−10 sccm is introduced into the cell via a one-quarter-inch stainless steel tube that terminates 1−2 cm in front of the outer surface of the cell wall. For nonvolatile molecules, a small copper oven (2 cm × 2 cm × 4 cm) is used to heat samples to produce sufficiently high vapor pressures. The oven, with an inner cavity of ~3 cm^3, is located *in vacuo* just outside

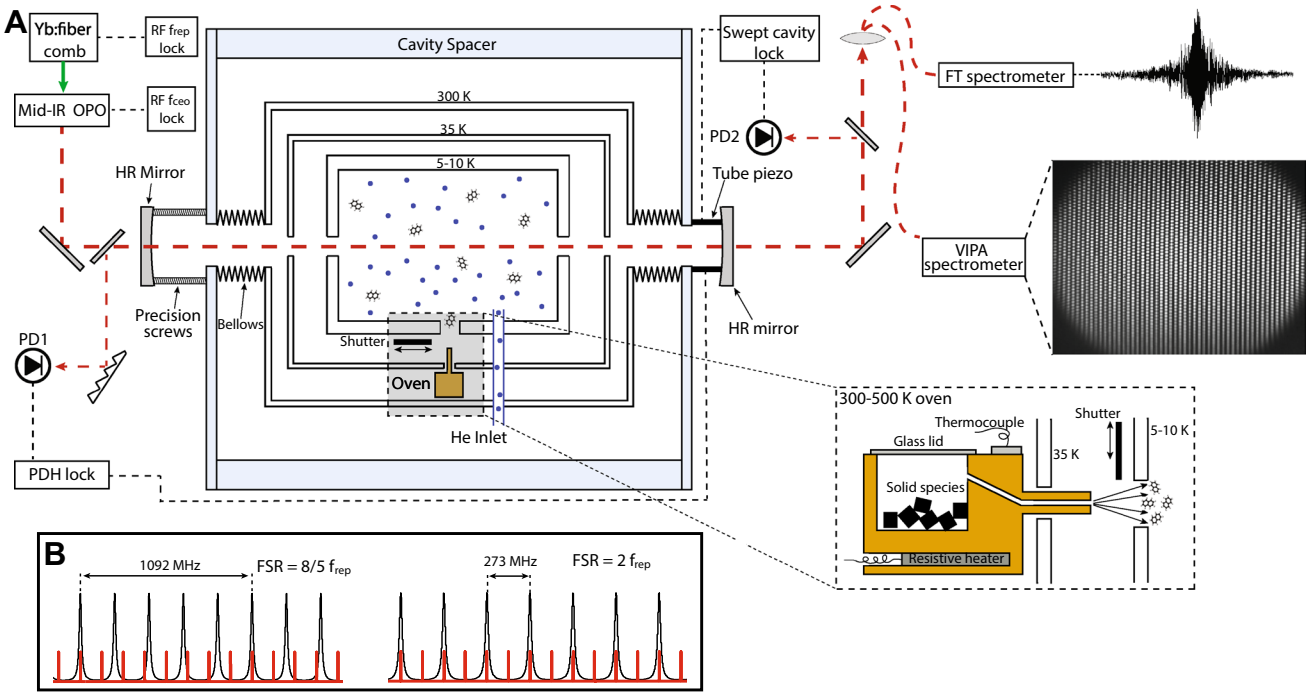

Fig. 1 Buffer gas cooling frequency comb spectrometer. **a** Schematic of the apparatus. Mid-infrared frequency comb light generated in the Yb fiber-pumped OPO is coupled to an enhancement cavity surrounding the cold cell dewar. RF locks stabilize the comb f_{ceo} and f_{rep} frequencies. The spectrum of the transmitted comb light is read out by an FT spectrometer, which measures a comb interferogram, or a VIPA spectrometer, which generates a two-dimensional image of dispersed comb modes. The cavity FSR is stabilized relative to the comb f_{rep} with a PDH or swept cavity lock. *Inset* illustrates the oven source used to introduce nonvolatile samples into the cold cell. **b** Cavity–comb filtering schemes. By adjusting the cavity FSR, an 8:5 (*left*) or 2:1 (*right*) f_{rep}-to-FSR ratio can be selected. Comb modes not resonant with the cavity are rejected, resulting in a sparser transmitted comb spectrum, which facilitates single comb mode resolution with the FTS or VIPA

the 35 K radiation shield, with a small tube outlet passing through the shield to guide molecules into the cold cell (see inset of Fig. 1a). The inner diameter (2 mm) and length (3 cm) of the outlet determine the output conductance of the oven and therefore what vapor pressure is necessary for sufficient molecule output flow. The output conductance is high enough to require only modest oven temperatures (100−200 °C), but small enough to allow sufficient oven pressure buildup to provide stable vaporization and prevent boiling. A small glass window permits visual monitoring of the interior of the oven while in use. The oven is resistively heated by two embedded cartridge heaters and temperature monitored by a thermocouple.

A "molecule shutter" consisting of a thin aluminum paddle is placed between the molecule tube or oven outlet and the cold cell aperture in order to quickly turn on or off the molecule flow into the cold cell. The shutter is rotated into and out of the molecule flow with a small DC electric motor mounted to the 35 K shield. Short current pulses switch the shutter with an open/close time of 1 ms and a delay of 10 ms.

In order to increase the effective interaction length of the comb light and the molecular absorbers, an enhancement cavity consisting of two parallel mirrors with high reflectivity (HR) coatings surrounds the cold cell. Four one-inch-thick stainless steel rods, girdling the cryostat dewar, fix the gross cavity length. The cavity mirrors are mechanically isolated from the dewar by a system of edge-welded bellows that form the vacuum connection between the cavity mirrors and the dewar. The position and alignment of each mirror are adjusted macroscopically by a set of fine precision screws. One of the cavity mirrors is fitted with a tube piezo for fine length adjustment and feedback control. The HR mirrors have a broadband coating covering 3.1−3.5 μm and a maximum finesse of $\mathcal{F} \approx 6000$. We typically achieve on-resonance cavity transmission efficiency of a few percent over a simultaneous transmission bandwidth of ~100 nm, limited by the HR mirror dispersion. Recent developments in mid-infrared mirror coatings [17] show that both the cavity finesse and transmission efficiency can be significantly improved, which provides direct benefits to the sensitivity of CE-DFCS.

2.3 Cavity–comb coupling and spectral readout schemes

We have implemented two different methods for coupling the infrared frequency comb to the enhancement cavity and

for reading out the transmitted comb light spectrum. The first of these uses a Pound–Drever–Hall (PDH) lock to match the cavity free spectral range (FSR) to the comb f_{rep}, while the spectrum of the continuous comb transmission is measured with a fast-scanning Fourier transform spectrometer (FTS) [6, 18, 19]. The second approach uses a swept cavity coupling scheme and a virtually imaged phased array (VIPA) spectrometer for readout [5, 20]. These approaches have different advantages in resolution and sensitivity, and depending on the conditions of the experiment one may be preferable over the other. The remainder of this section describes each method in detail and compares their performance.

2.3.1 PDH cavity lock and FTS readout

A PDH lock permits the cavity and comb to be resonantly coupled continuously, resulting in the highest cavity transmission duty cycle. Phase modulation sidebands are generated by dithering the fiber laser oscillator cavity length at 760 kHz, which corresponds to a resonance in the fiber oscillator mirror piezo. Light reflected from the cold cell enhancement cavity is picked off with a magnesium fluoride flat, dispersed with a reflection grating, passed through a slit, and incident on a photodiode. The grating and slit allow only a ∼10-nm portion of the comb light to reach the photodiode. The photodiode signal is then demodulated at the 760 kHz dither frequency to generate a PDH error signal. This error signal is used to servo the enhancement cavity length via the tube piezo to ensure the cavity FSR matches the comb f_{rep}. The PDH error signal is used to feed back in parallel on the fiber laser oscillator piezo at fast timescales, which helps to extend the effective servo bandwidth beyond the response of the enhancement cavity tube piezo (∼1 kHz). Due to dispersion in the cavity, its optical resonance frequencies have a DC offset $f_{0,\mathrm{cav}}$ ($0 \leq f_{0,\mathrm{cav}} < \mathrm{FSR}$), analogous to the comb f_{ceo} frequency. We obtain the widest PDH lock transmission bandwidth by setting $f_{\mathrm{ceo}} = f_{0,\mathrm{cav}}$. However, we typically detune f_{ceo} from $f_{0,\mathrm{cav}}$ by up to a few MHz, which we observe decreases the cavity transmission intensity noise, albeit at the cost of reduced transmission bandwidth.

The transmitted comb light is routed to a home-built fast-scanning FTS [19]. An example of the center burst of a comb interferogram is illustrated in Fig. 1a. Each arm of the interferometer is double passed on a translating corner-cube retroreflector. This geometry multiplies the physical scanning range of the FTS delay stage (0.7 m) by a factor of four, to yield interferograms with a net optical path length difference of $\ell = 2.8$ m. The corresponding spectrometer linewidth is $\Delta\nu_{\mathrm{FTS}} = c/\ell = 110$ MHz. For a traditional white light source, this would determine the fundamental resolution limit of the FTS. However, the situation can be very different with an optical frequency comb: If adjacent comb modes are individually resolved by the spectrometer, then the effective resolution is determined by the linewidth of the comb mode (typically ∼50 kHz), instead of that of the spectrometer [21]. This condition is met if the spectrometer resolution is narrower than the comb mode spacing. As our repetition rate $f_{\mathrm{rep}} = 136.6$ MHz is only slightly larger than $\Delta\nu_{\mathrm{FTS}}$, we set the length of the enhancement cavity such that the cavity FSR $= 2f_{\mathrm{rep}}$. This has the effect of filtering out every other comb mode, as illustrated in the right half of Fig. 1b, resulting in a transmitted comb mode spacing of $2f_{\mathrm{rep}} = 273$ MHz, which is readily resolved by the FTS.

Because the cavity FSR is not an integer multiple of $\Delta\nu_{\mathrm{FTS}}$, the transmitted comb mode frequencies and the center frequencies of the Fourier transform spectrum walk off with respect to one another. In order to measure the spectrum at the actual comb mode frequencies, we resample the complex-valued frequency spectrum via convolution with the known instrument lineshape function (a sinc function). In this manner, we can efficiently locate the center frequency and intensity of each comb mode. The absolute frequency calibration of the spectrum is performed by measuring known transition frequencies of calibrant molecules, typically CH_4, which provide a ∼30 MHz absolute accuracy. The relative frequency accuracy is 5−10 MHz, limited by the f_{rep} scan step size (see below).

The filtered comb mode spacing of 273 MHz is much larger than the typical Doppler linewidths of the cold molecules ($\Delta\nu_{\mathrm{mol}} \approx 20-60$ MHz). Therefore, for a given cavity FSR, a single FTS acquisition will only measure a fraction of the molecular absorption transitions. In order to fill in the gaps, multiple spectra are acquired at slightly different comb f_{rep} values (and corresponding cavity FSRs), spaced apart by Δf_{rep}. The shift in the optical frequency of each comb mode is $\Delta\nu_n = n\Delta f_{\mathrm{rep}}$, where $n \approx 10^5-10^6$ is the comb mode number. We typically choose Δf_{rep} such that $n\Delta f_{\mathrm{rep}} < \Delta\nu_{\mathrm{mol}}/5$. FTS acquisitions at each value of Δf_{rep} are then interleaved together to form a single high-resolution spectrum. To obtain an absorption spectrum, we separately normalize out the slowly varying transmission spectrum for each FTS acquisition. This baseline is obtained by simply applying a low-pass filter to the measured FTS spectrum. In the absence of severe spectral congestion, molecular absorption features, with 20−60 MHz Doppler-limited linewidths, can be clearly distinguished from broader fluctuations across the comb spectrum. Etalons and shot-to-shot fluctuations in the measured comb spectrum, which are typically observed with characteristic widths of 2−300 GHz, are completely removed by this normalization process. A single interferogram can be collected and processed in 5−10 s. An entire f_{rep}-stepped spectrum, with four averages per f_{rep} value, requires 30 min of scanning

time. Because of the massively multiplexed nature of the frequency comb, this represents an orders-of-magnitude improvement in "spectral velocity" relative to state-of-the-art single frequency cw laser spectroscopy [10].

The fundamental limit to the absorption sensitivity is set by the photon shot noise. For the comb powers used here, this limit is about 10^{-4} $Hz^{-1/2}$ fractional absorption for a single spectral element of the Fourier transform spectrum, which is well below our measured noise floor. In the PDH/FTS configuration, our dominant noise is intensity fluctuations of cavity-transmitted comb light, caused mostly by the unfavorable frequency-to-amplitude noise conversion by the cavity. An autobalanced detector circuit that measures both output arms of the FTS interferometer reduces the common mode intensity noise by up to 20 dB at the interferogram carrier frequency (100−200 kHz). However, residual intensity noise remains the largest noise source, resulting in an absorption sensitivity limit of 4.4×10^{-8} cm^{-1} $Hz^{-1/2}$ for a single comb mode. The typical bandwidth of the FTS spectra contains 3300 resolved comb lines, corresponding to 7.6×10^{-10} cm^{-1} $Hz^{-1/2}$ per spectral element (PSE). This is roughly an order of magnitude worse than previous trace detection experiments using mid-infrared CE-DFCS, which reported a sensitivity of 6.9×10^{-11} cm^{-1} $Hz^{-1/2}$ PSE [6]. This discrepancy is accounted for by our narrower cavity linewidth and transmission bandwidth, as well as increased cavity length noise. We note that while the enhancement cavity is ~60 cm long, we only make use of 6 cm (the length of the cold cell) where molecules are present. Consequently, we suffer from a narrow cavity linewidth and therefore increased frequency-to-amplitude noise conversion, without the compensation in sensitivity provided by a longer path length.

2.3.2 *Swept cavity lock and VIPA readout*

Given that the PDH/FTS absorption sensitivity is limited by cavity transmission noise, an amplitude noise immune cavity locking scheme can potentially provide significant sensitivity improvements. Such a scheme is realized by the swept cavity lock method [5]. Here, the enhancement cavity length is scanned by applying a 10 kHz modulation signal to the cavity tube piezo. As the cavity length is swept, it passes through resonance with the incident comb light, permitting a transient buildup and transmission of power over the entire comb bandwidth. A regular sequence of transmission bursts, occurring at twice the sweep frequency, exits the cavity as the cavity length is scanned back and forth. The relative time spacing between sequential transmission bursts is determined by the offset between the resonant cavity length and the mean value of the cavity length scan range. A small fraction of the transmitted cavity light is measured by a photodiode, and this signal is demodulated at the sweep frequency via a lock-in amplifier, generating an error signal that is fed back onto the cavity length tube piezo. The feedback loop only requires that the resonant cavity length remains near the middle of the tube piezo scan range. Therefore, this locking scheme only requires a ~1 kHz servo loop bandwidth with no feedback on the fiber comb.

Unfortunately, the pulsed nature of the swept cavity transmission is incompatible with the FTS readout. The interferogram is digitized at a sampling rate of 8 MHz, which is significantly higher than the maximum cavity length sweep frequency. Consequently, there is no way to synchronize the FTS sampling with the intermittent cavity transmission. As an alternative to the FTS, we use a dispersive mid-IR VIPA spectrometer [20]. In brief, the spectrometer consists of an HR-coated parallel plate etalon, which disperses the comb light strongly in the vertical direction, resulting in spatially resolved comb modes, followed by a reflective grating, which separates out FSRs of the etalon in the horizontal direction. The two-dimensional pattern of comb light is then imaged onto a liquid N_2 cooled InSb array detector. We integrate the detector pixel counts for 2 ms per frame, corresponding to collecting light from 40 swept cavity transmission bursts.

The VIPA etalon has a resolution of 600 MHz. Therefore, the 2:1 f_{rep}-to-FSR cavity filtering used with the FTS is insufficient for comb mode-resolved spectra. Instead, we increase the enhancement cavity length to perform filtering with an 8:5 f_{rep}-to-FSR ratio, as illustrated in the left of Fig. 1b. The cavity-transmitted comb lines are spaced in this configuration by $8f_{rep} \approx 1093$ MHz, which can be well resolved by the VIPA spectrometer. A raw camera image displaying an array of individually resolved comb modes is shown in Fig. 1. Due to the Lorentzian lineshape of the VIPA etalon, the relatively wide tails of the imaged comb modes partially overlap with neighboring modes, resulting in spectral "crosstalk." After processing the image to extract the absorption spectrum, this crosstalk appears as artificial absorption lines spaced from the real lines by exactly the comb mode spacing ($8f_{rep}$). When optimally aligned, the amplitude of these features is approximately 3% relative to the real feature. We also apply an active correction filter to further reduce spectral crosstalk. This is performed by subtracting from the spectrum the expected crosstalk contributions from absorption features stronger than a given threshold. To do this, one must know the relative size of crosstalk peaks to the real peak, which is separately measured using a sparsely absorbing calibrant molecule such as methane. This active correction filter further reduces spectral crosstalk to 0.5%. In the absence of very strong absorption features, these artifacts are below our noise floor and do not obstruct the interpretation of our spectra.

The VIPA spectrometer camera frame rate (max. 435 Hz) permits rapid readout of successive spectra, enabling us to perform fast differential absorption measurements to further reduce the absorption noise baseline. Using the molecule shutter described above, we block molecules from entering the cold cell and acquire a reference light spectrum with the VIPA spectrometer. Then the molecule shutter is opened, permitting absorbers to enter the cold cell and another spectrum is acquired. The fractional absorption spectrum is computed from the relative change in the comb mode intensities. Given the diffusion time in the cell (∼10 ms), we perform this differential measurement in 40 ms periods (50% molecules on, 50% molecules off). The reduction of the light intensity noise as a function of the switching time is illustrated in Fig 2a. At the switching times comparable to the camera frame rate, the noise curve begins to plateau, indicating that the camera background noise limit has been reached. At this limit, we achieve an absorption sensitivity ∼ten times smaller than the previous PDH/FTS limit. This represents a 20-fold improvement in the cavity transmission noise floor, but the swept cavity lock introduces a factor of 1/2 to the enhancement cavity's effective path length [5]. An example of the baseline noise reduction in actual spectra is shown in Fig 2b.

As with the PDH/FTS scheme, the comb f_{rep} and cavity FSR must be scanned to cover the spectral range between transmitted comb modes. One disadvantage of the poorer VIPA spectrometer resolution is that the 8:5 cavity filtering requires a 4× longer scanning range than the 2:1 filtering. However, because of the improved sensitivity of the swept cavity lock/VIPA spectrometer, and because the camera frame acquisition time is much shorter than the FTS scanning time, we average for less time per f_{rep} value, resulting in a similar total acquisition time of 30 min. Also, the rapid differential absorption measurements allowed by this spectrometer remove etalons from the computed absorption spectrum. Laser amplitude fluctuations produce small, broad variations across the baseline of the absorption spectrum. We remove these variations by separately fitting the baseline of each acquired spectrum.

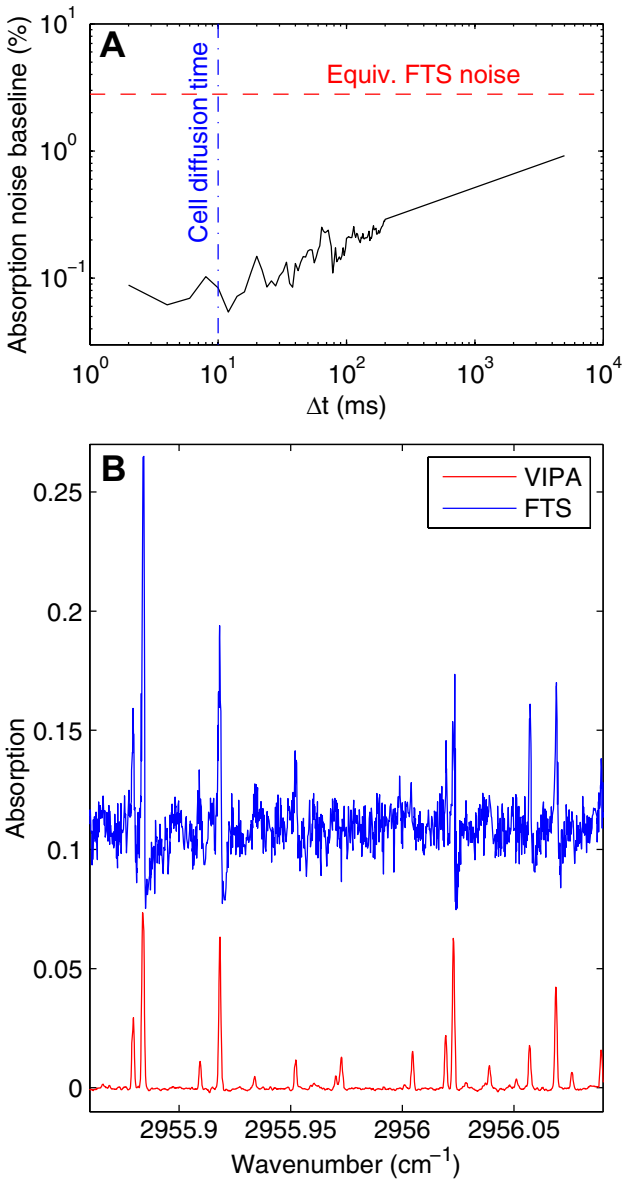

Fig. 2 Absorption noise baseline comparison of FTS versus VIPA. **a** The VIPA spectrometer absorption noise baseline as a function of the differential light intensity measurement period is plotted as the *black solid trace*. Each measurement used a total integration time of 5 ms. The equivalent time FTS noise baseline is also indicated (*red horizontal dashed line*), as well as the molecule diffusion time in the cold cell (*blue vertical dashed line*). **b** A small portion of the absorption spectrum of nitromethane (CH_3NO_2) near 2956 cm^{-1}, comparing the noise baseline of the FTS spectrum (*blue*, shifted up) and the VIPA spectrum (*red*, bottom trace). Both spectra were gathered with a 30 min total acquisition time

3 Spectroscopy of polyatomic molecules

3.1 Vinyl bromide

The 3 μm region of the absorption spectrum of vinyl bromide, CH_2CHBr, is dominated by the CH stretching fundamentals. All three CH stretching modes are IR active, and all three are readily observed in the spectrum spanning the region 3020−3120 cm^{-1}. As a demonstration of both the resolution and accurate intensities provided by the spectrometer, we discuss in detail only the spectrum of the ν_3 fundamental, which has the lowest frequency of the three CH stretches. An overview of the ν_3 band is shown in Fig. 3a. This mode is assigned as the in-phase stretching vibration of the two hydrogens on the CH_2 end of the molecule [22, 23].

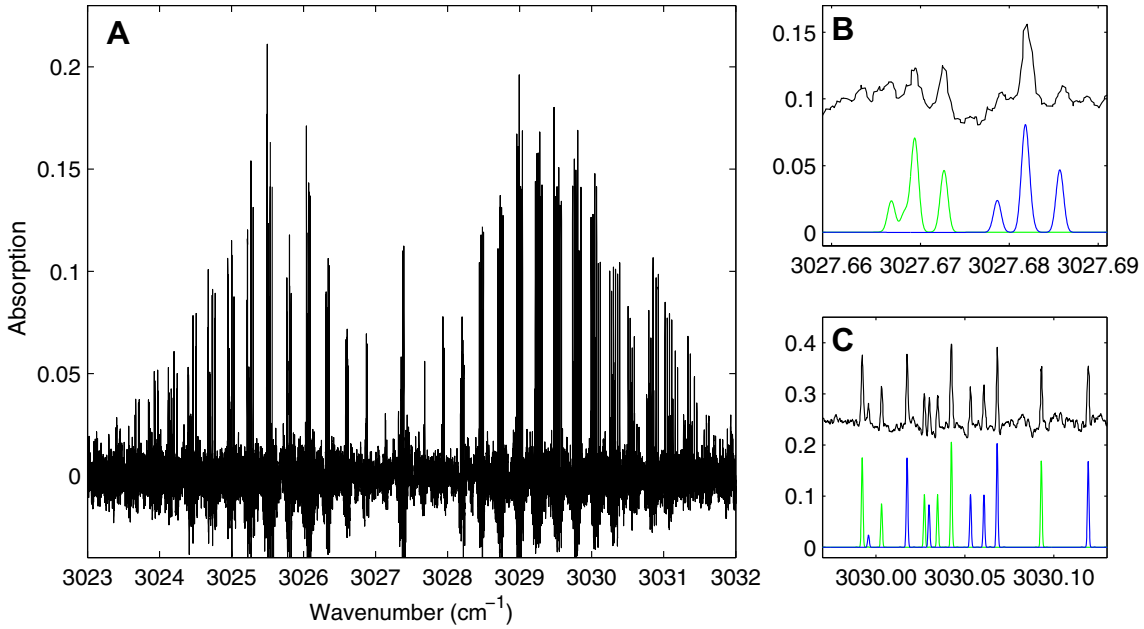

Fig. 3 Vinyl bromide ν_3 band. **a** Overview of the ν_3 spectrum acquired with the PDH/FTS technique. **b** Hyperfine splittings of the $R(0)$ transition. The measured spectrum is shown in *black*, with a vertical offset. The simulated spectra of $CH_2CH^{79}Br$ (*blue*) and $CH_2CH^{81}Br$ (*green*) are shown below. The three hyperfine components correspond to transitions from a common $F'' = 3/2$ lower state to upper states with $F' = 1/2$, $5/2$, and $3/2$, in order of increasing transition frequency. **c** Measured and simulated spectra of the $R(9)$ transitions. The multiple transitions belong to different K sub-bands and parity components with $K = 0$–4

Vinyl bromide is a relatively rigid, near-prolate top [24–26]. The otherwise straightforward appearance of its spectrum is, however, complicated by the bromine atom, which occurs as two main isotopes, ^{79}Br and ^{81}Br. Each has approximately 50% natural abundance, and thus, there are two equally strong vibrational bands superimposed in the spectrum, resulting in increased congestion and line density. Additionally, both bromine isotopes have a nuclear spin of $I = 3/2$ and a relatively large nuclear electric quadrupole moment. As a result, hyperfine structure in the spectrum is observable, especially in the low J transitions. An example of these hyperfine splittings for the $R(0)$ transition of each isotopologue is shown in Fig. 3b.

With the aid of known ground-state combination differences measured by rotational microwave spectroscopy [26], we assigned several hundred rovibrational transitions involving rotational levels up to $J \leq 18$. Using the PGOPHER program [27], we performed a fit to an effective rotational Hamiltonian for each isotopologue. The results of these fits are summarized in Table 1. The average fit error of 6 MHz is consistent with our relative line center measurement uncertainty. Moreover, as shown in Fig. 3c, the simulated relative transition intensities agree very well with the experimental spectrum, and we observe no perturbations to the measured transitions.

The hyperfine splittings, observed most clearly in the $R(0)$ and $P(1)$ transitions of each isotopologue, indicate that the nuclear quadrupole coupling constants do not change significantly between the vibrational ground and excited states. This is consistent with the expectation that this CH stretching mode does not include relative motion between the bromine atom and the carbon atom it forms a bond with. The electric field gradient at the bromine nucleus is therefore relatively unaffected by excitation in ν_3.

All three CH stretching modes, being in-plane motions, can in principle have a transition dipole projection along both the a and b principal axes. However, we have not yet identified any b-type transitions, readily discerned by their $\Delta K_a =$ odd selection rule, in the ν_3 spectrum. We estimate the ratio of the transition dipole components to be $|\mu_b/\mu_a|^2 < 0.1$, i.e., that the ν_3 transition dipole is aligned closely along the a axis. A simple model would be to assume that the vibrational transition dipole is approximately the vector sum of the oscillating dipoles of each local CH stretch. If both of the CH_2 stretches contribute equally to the ν_3 normal mode, then the transition dipole would be approximately parallel to the C=C double bond, which has a non-negligible projection along the b axis. Instead, the measured spectrum suggests that the ν_3 mode contains a larger contribution from the CH stretch *trans* to the C−Br bond and a lesser contribution from the CH stretch *cis* to the C−Br bond.

In summary, the frequency and intensity information contained in our CE-DFCS spectrum provides

Table 1 Vinyl bromide effective Hamiltonian fits for the ν_3 band of $CH_2CH^{79}Br$ and $CH_2CH^{81}Br$

Parameter		^{79}Br		^{81}Br	
		$v = 0$	ν_3	$v = 0$	ν_3
ν_0		0	3027.4152 (10)	0	3027.4041 (10)
A		1.810093	1.804461 (7)	1.809641	1.804053 (9)
B		0.1388471	0.1387183 (4)	0.1380359	0.1379096 (5)
C		0.1288373	0.1286733 (5)	0.1281362	0.1279755 (5)
Δ_J	$\times 10^7$	0.534	0.520 (12)	0.528	0.553 (13)
Δ_{JK}	$\times 10^5$	−0.10216	−0.1188(29)	−0.10146	−0.1018 (47)
Δ_K	$\times 10^4$	0.4223	0.1624 (40)	0.4206	0.2835 (51)
δ_J	$\times 10^8$	0.57	[0.57]	0.57	[0.57]
δ_K	$\times 10^6$	0.3922	[0.3922]	0.3841	[0.3841]
χ_{aa}		470.98	469.55 (237)	393.58	394.13 (237)
χ_{bb-cc}		37.04	31.59 (733)	30.86	22.68 (716)
$\lvert\chi_{ab}\rvert$		246.14	[246.14]	204.17	[204.17]
RMS error $\times 10^4$			2.20		2.24

The standard Watson A-reduced quartic Hamiltonian (I^r representation) was used to fit the measured transition frequencies. All values are given in cm^{-1}, except for χ_{aa}, χ_{bb-cc}, and $|\chi_{ab}|$, which are given in MHz. All ground-state ($v = 0$) constants are taken from Ref. [24], again except for χ_{aa}, χ_{bb-cc}, and $|\chi_{ab}|$, which are taken from Ref. [26]. Values in [] brackets are held fixed during the fit. 1σ uncertainties are specified in parentheses; for ν_0 values, the uncertainty corresponds to the estimated absolute frequency accuracy of our calibration procedure

complementary insights into how the electronic properties of vinyl bromide are changed upon excitation in the ν_3 normal mode. The measured nuclear hyperfine structure indicates the C−Br bond is unaffected by this vibration, while the relative strengths of rovibrational transitions illustrate that the electric charge distribution oscillates nearly parallel to the *a* axis.

3.2 Large hydrocarbons: adamantane and diamantane

Extending the domain of high-resolution infrared spectroscopy to large molecules is only possible if individual rovibrational transitions can be well resolved in a given vibrational band. Several factors determine the degree of spectral congestion. These can be classified as either extrinsic effects (those that depend on the experimental conditions) or intrinsic effects (those determined by inherent molecular properties, such as rotational line spacing and IVR).

The low translational and rotational temperatures afforded by buffer gas cooling significantly reduce spectral congestion caused by extrinsic effects, namely by reducing the Doppler broadened linewidth and the rotational partition function. At the conditions of our experiment, the linewidth decreases with temperature as $T^{1/2}$ and the rotational partition function as $T^{3/2}$. At 15 K, this yields improvements by factors of 4.5 and 90, respectively, relative to room temperature. Not only does this significantly reduce spectral congestion, but also offers an orders-of-magnitude increase in peak absorption cross sections.

We have exploited these benefits to measure the first rotationally resolved absorption spectra in the CH stretching region of adamantane, $C_{10}H_{16}$, a large hydrocarbon that serves as the basic building block of "diamonoids," carbon cage molecules with the structure of the diamond lattice. Spectra from our recent initial report [8] are shown in Fig. 4a. Instead of single $R(J)$ or $P(J)$ rotational transitions, as expected from a rigid spherical top, the rotational transitions are split into dense clusters of lines by non-spherical centrifugal distortion effects allowed by the lower tetrahedral symmetry of the molecule. The detailed patterns observed in the spectrum report on subtle aspects of the rovibrational structure. Due to the spectroscopic selection rules of tetrahedral tops, transition combination differences cannot be obtained from the infrared active fundamentals [28], complicating the analysis. We thus forego further discussion of fitting transition frequencies of adamantane here.

The obvious question is: How large can one go? While the answer depends on detailed properties of an individual molecule in addition to just its size, a natural comparison to adamantane is diamantane, $C_{14}H_{20}$, the next largest member of the diamonoid family. Using an ab initio equilibrium geometry [29], we estimate diamantane's rotational constants to be $A = 0.0423\ cm^{-1}$ and $B = C = 0.0258\ cm^{-1}$. In the absence of anharmonic or rovibrational perturbations, rigid symmetric top simulations using these

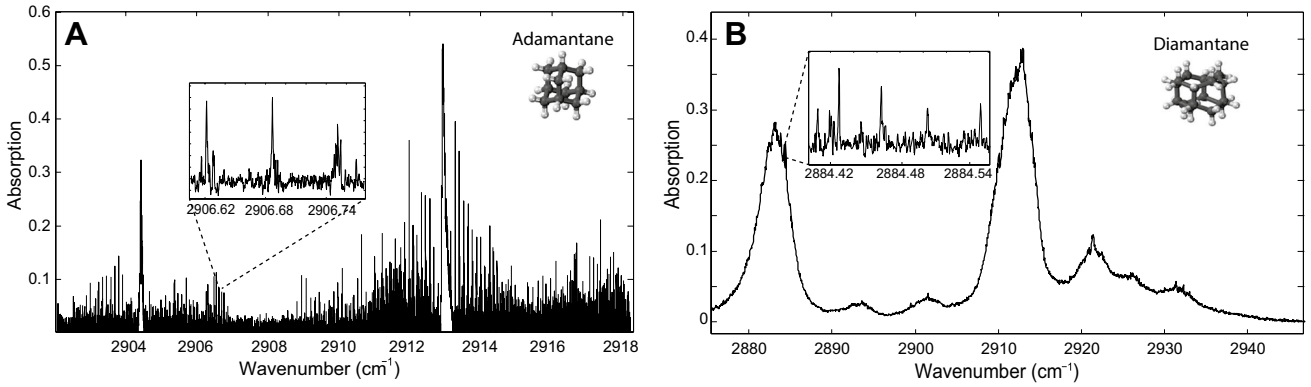

Fig. 4 Mid-infrared spectra of diamonoids. **a** A portion of the CH stretching manifold of adamantane. This spectrum was recorded with the PDH/FTS scheme. *Inset* shows resolved rotational fine structure. **b** The absorption spectrum of diamantane in the CH stretching region, acquired with the swept cavity/VIPA technique. At our experimental conditions, the spectrum is essentially continuous, with no well-resolved rotational structure. *Inset* shows the rare appearance of narrow features above the continuous background (*inset* spectrum has been high-pass filtered for visual clarity). The width of these features is consistent with the expected Doppler broadened linewidth, and the spacing between them is approximately equal to $2B$

rotational constants display dense, yet rotationally resolved, mid-infrared vibrational bands. The measured absorption spectrum of diamantane in the CH stretch region is shown in Fig 4b. While measured at the same experimental conditions as that of adamantane, the spectrum of diamantane shows no clearly resolved structure and is essentially continuous. A limited number of narrow features appearing above the background absorption indicate that the Doppler linewidth is as narrow as expected (20 MHz at 20 K). These features are spaced by approximately 0.05 $cm^{-1} \approx 2B$ and mostly likely correspond to sequential $R(J)$ transitions of a rotational branch. Furthermore, the widths of the rotational contours suggest a rotational temperature in the range 10−30 K. These observations indicate that the buffer gas cooling of this molecule is just as efficient as for adamantane.

We therefore attribute the failure to observe well-resolved rotational fine structure as an indication of intrinsic congestion caused by IVR. An important parameter in determining the severity of IVR is the vibrational density of states at the internal energy of the excited vibrational state. As illustrated in Fig. 5, the total density of vibrational states near 3000 cm^{-1} is roughly an order of magnitude larger for diamantane versus adamantane. This is apparently enough to move diamantane over the congestion threshold, with the spectroscopic bright state character of the CH stretching fundamental distributed over many densely spaced eigenstates, all of which contribute to the continuous absorption spectrum.

The caged structure of diamantane leads to a relatively rigid nuclear framework. A general molecule of this size or larger will typically be less rigid and have lower vibrational frequencies, resulting in significantly higher vibrational state

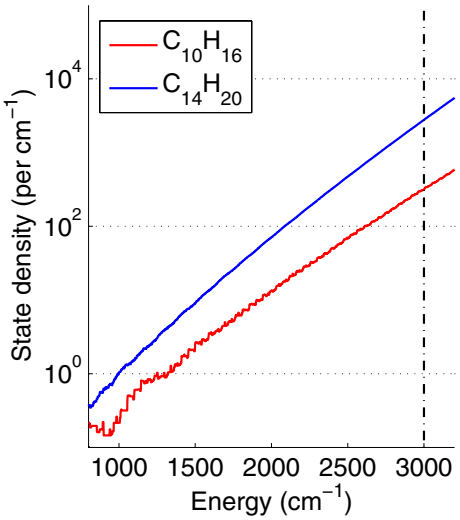

Fig. 5 Vibrational state density. The estimated density of vibrational states per cm^{-1} is plotted against vibrational energy for adamantane, $C_{10}H_{16}$, (*red*) and diamantane, $C_{14}H_{20}$, (*blue*). The *vertical dashed line* corresponds to the approximate internal energy probed in this study. The state densities are calculated using a direct state counting method [30] as done in Ref. [8]

densities at a given internal energy. While a few remarkable exceptions exist, like the highly symmetric dodecahedrane, $C_{20}H_{20}$ [31], our expectation is that in general high-resolution rovibrational spectroscopy of large molecules will have to be conducted at longer wavelengths, probing molecules at lower internal energies. Such approaches with cw laser spectroscopy have found success [10, 32]. Recent and ongoing development of frequency comb technology beyond 5 μm [33–37] will enable direct frequency comb spectroscopy in these wavelength regions.

4 Conclusions

We have used cavity-enhanced direct frequency comb spectroscopy of buffer gas cooled molecules to obtain the first high-resolution rovibrational spectra of several large complex molecules in the CH stretch region, providing new and detailed insights into their molecular structure. High-resolution spectroscopy in the 3 μm region is ultimately limited by intrinsic spectral congestion in the largest molecules studied here. We are currently developing new frequency comb systems in the longer IR wavelength regions, and we plan to use these to investigate even larger systems, such as C_{60}. Another promising future direction is the study of reactive species in the cryogenic buffer gas cell environment. Our high-sensitivity, broadband absorption technique presents the possibility of studying chemical kinetics at low thermal energies over long interrogation times via time-resolved frequency comb spectroscopy [7]. Such measurements would have direct and significant relevance to our understanding of atmospheric and interstellar chemistry.

Acknowledgements We dedicate this paper to Ted Hänsch, who has pioneered the field of laser spectroscopy in general and optical frequency combs in particular. This research was funded by DARPA SCOUT, AFOSR, NIST, and NSF-JILA PFC. P.B.C. is supported by the NSF GRFP (Award no. DGE1144083). B.S. is supported through an NRC Postdoctoral Fellowship. D.P. and J.M.D. acknowledge additional support from the NSF. We would like to thank Matthew Radzihovsky for experimental assistance at JILA.

References

1. T. Udem, R. Holzwarth, T.W. Hänsch, Optical frequency metrology. Nature **416**, 233–237 (2002)
2. S.T. Cundiff, J. Ye, Colloquium : femtosecond optical frequency combs. Rev. Mod. Phys. **75**, 325–342 (2003)
3. M.C. Stowe, M.J. Thorpe, A. Pe'er, J. Ye, J.E. Stalnaker, V. Gerginov, S.A. Diddams, Direct frequency comb spectroscopy. Adv. At. Mol. Opt. Phys. **55**, 1–60 (2008)
4. M. Thorpe, J. Ye, Cavity-enhanced direct frequency comb spectroscopy. Appl. Phys. B **91**, 397–414 (2008)
5. F. Adler, M.J. Thorpe, K.C. Cossel, J. Ye, Cavity-enhanced direct frequency comb spectroscopy: technology and applications. Annu. Rev. Anal. Chem. **3**, 175–205 (2010)
6. A. Foltynowicz, P. Masłowski, A.J. Fleisher, B.J. Bjork, J. Ye, Cavity-enhanced optical frequency comb spectroscopy in the mid-infrared application to trace detection of hydrogen peroxide. Appl. Phys. B **110**, 163–175 (2012)
7. A.J. Fleisher, B.J. Bjork, T.Q. Bui, K.C. Cossel, M. Okumura, J. Ye, Mid-infrared time-resolved frequency comb spectroscopy of transient free radicals. J. Phys. Chem. Lett. **5**, 2241–2246 (2014)
8. B. Spaun, P.B. Changala, D. Patterson, B.J. Bjork, O.H. Heckl, J.M. Doyle, J. Ye, Continuous probing of cold complex molecules with infrared frequency comb spectroscopy. Nature **533**, 517–520 (2016)
9. S. Davis, D.T. Anderson, G. Duxbury, D.J. Nesbitt, Jet-cooled molecular radicals in slit supersonic discharges: Sub-Doppler infrared studies of methyl radical. J. Chem. Phys. **107**, 5661 (1997)
10. B.E. Brumfield, J.T. Stewart, B.J. McCall, Extending the limits of rotationally resolved absorption spectroscopy: pyrene. J. Phys. Chem. Lett. **3**, 1985–1988 (2012)
11. J.K. Messer, F.C. De Lucia, Measurement of pressure-broadening parameters for the CO-He system at 4 K. Phys. Rev. Lett. **53**, 2555–2558 (1984)
12. D. Patterson, E. Tsikata, J.M. Doyle, Cooling and collisions of large gas phase molecules. Phys. Chem. Chem. Phys. **12**, 9736–9741 (2010)
13. D. Patterson, J.M. Doyle, Cooling molecules in a cell for FTMW spectroscopy. Mol. Phys. **110**, 1757–1766 (2012)
14. J. Piskorski, D. Patterson, S. Eibenberger, J.M. Doyle, Cooling, spectroscopy and non-sticking of trans-stilbene and Nile Red. Chemphyschem **15**, 3800–4 (2014)
15. D.J. Nesbitt, R.W. Field, Vibrational energy flow in highly excited molecules: role of intramolecular vibrational redistribution. J. Phys. Chem. **100**, 12735–12756 (1996)
16. F. Adler, K.C. Cossel, M.J. Thorpe, I. Hartl, M.E. Fermann, J. Ye, Phase-stabilized, 1.5 W frequency comb at 2.8−4.8 μm. Opt. Lett. **34**, 1330 (2009)
17. G.D. Cole, W. Zhang, B.J. Bjork, D. Follman, P. Heu, C. Deutsch, L. Sonderhouse, J. Robinson, C. Franz, A. Alexandrovski, M. Notcutt, O.H. Heckl, J. Ye, M. Aspelmeyer, High-performance near- and mid-infrared crystalline coatings. Optica **3**, 647 (2016)
18. J. Mandon, G. Guelachvili, N. Picqué, Fourier transform spectroscopy with a laser frequency comb. Nat. Photon. **3**, 99–102 (2009)
19. F. Adler, P. Masłowski, A. Foltynowicz, K.C. Cossel, T.C. Briles, I. Hartl, J. Ye, Mid-infrared Fourier transform spectroscopy with a broadband frequency comb. Opt. Express **18**, 21861–72 (2010)
20. L. Nugent-Glandorf, T. Neely, F. Adler, A.J. Fleisher, K.C. Cossel, B. Bjork, T. Dinneen, J. Ye, S.A. Diddams, Mid-infrared virtually imaged phased array spectrometer for rapid and broadband trace gas detection. Opt. Lett. **37**, 3285 (2012)
21. P. Maslowski, K.F. Lee, A.C. Johansson, A. Khodabakhsh, G. Kowzan, L. Rutkowski, A.A. Mills, C. Mohr, J. Jiang, M.E. Fermann, A. Foltynowicz, Surpassing the path-limited resolution of Fourier-transform spectrometry with frequency combs. Phys. Rev. A **93**, 021802 (2016)
22. D. McKean, CH stretching frequencies, bond lengths and strengths in halogenated ethylenes. Spectrochim. Acta Part A Mol. Spectrosc. **31**, 1167–1186 (1975)
23. N. Zvereva-Loëte, J. Demaison, H. Rudolph, Ab initio anharmonic force field and equilibrium structure of vinyl bromide. J. Mol. Spectrosc. **236**, 248–254 (2006)
24. D. de Kerckhove Varent, Contribution a l'etude de la molecule de bromure de vinyle en spectroscopie hertzienne. II. Bromure de vinyle monodeutere et substitue en 13C, second ordre du couplage quadripolaire, structure de la molecule. Ann. Soc. Sci. Brux. **T84**, 277–292 (1970)
25. A. Pietropolli Charmet, P. Stoppa, A. Baldacci, S. Giorgianni, S. Ghersetti, Diode laser spectrum and rovibrational study of the ν_6 fundamental of vinyl bromide. J. Mol. Struct. **612**, 213–221 (2002)
26. M. Hayashi, C. Ikeda, T. Inagusa, Microwave spectrum, structure, and nuclear quadrupole coupling constant tensor of vinyl bromide and iodide. J. Mol. Spectrosc. **139**, 299–312 (1990)
27. PGOPHER, A program for simulating rotational, vibrational and electronic spectra, C. M. Western, University of Bristol. http://pgopher.chm.bris.ac.uk
28. O. Pirali, V. Boudon, J. Oomens, M. Vervloet, Rotationally resolved infrared spectroscopy of adamantane. J. Chem. Phys. **136**, 024310 (2012)
29. J. Oomens, N. Polfer, O. Pirali, Y. Ueno, R. Maboudian, P.W. May, J. Filik, J.E. Dahl, S. Liu, R.M. Carlson, Infrared

spectroscopic investigation of higher diamondoids. J. Mol. Spectrosc. **238**, 158–167 (2006)
30. T. Baer, W.L. Hase, *Unimolecular Reaction Dynamics* (Oxford University Press, New York, 1996)
31. B.S. Hudson, D.G. Allis, S.F. Parker, A.J. Ramirez-Cuesta, H. Herman, H. Prinzbach, Infrared, Raman, and inelastic neutron scattering spectra of dodecahedrane: an I(h) molecule in T(h) site symmetry. J. Phys. Chem. A **109**, 3418–24 (2005)
32. S.K. Tokunaga, R.J. Hendricks, M.R. Tarbutt, B. Darquié, High-resolution mid-infrared spectroscopy of buffer-gas-cooled methyltrioxorhenium molecules (2016), arXiv:1607.08741
33. S.M. Foreman, D.J. Jones, J. Ye, Flexible and rapidly configurable femtosecond pulse generation in the mid-IR. Opt. Lett. **28**, 370 (2003)
34. A. Ruehl, A. Gambetta, I. Hartl, M.E. Fermann, K.S.E. Eikema, M. Marangoni, Widely-tunable mid-infrared frequency comb source based on difference frequency generation. Opt. Lett. **37**, 2232 (2012)
35. A. Gambetta, N. Coluccelli, M. Cassinerio, D. Gatti, P. Laporta, G. Galzerano, M. Marangoni, Milliwatt-level frequency combs in the $8-14\mu$m range via difference frequency generation from an Er:fiber oscillator. Opt. Lett. **38**, 1155 (2013)
36. Q.Y. Lu, M. Razeghi, S. Slivken, N. Bandyopadhyay, Y. Bai, W.J. Zhou, M. Chen, D. Heydari, A. Haddadi, R. McClintock, M. Amanti, C. Sirtori, High power frequency comb based on mid-infrared quantum cascade laser at $\lambda \sim 9\mu$m. Appl. Phys. Lett. **106**, 051105 (2015)
37. K.F. Lee, C.J. Hensley, P.G. Schunemann, M.E. Fermann, Difference frequency generation in orientation-patterned gallium phosphide. In *Conf. Lasers Electro-Optics*, page STu1Q.3. OSA, Washington, D.C. (2016). ISBN 978-1-943580-11-8